Volume 15 | Number 41 | 7 November 2019 | Pages 8187–8414

Soft Matter

rsc.li/soft-matter-journal

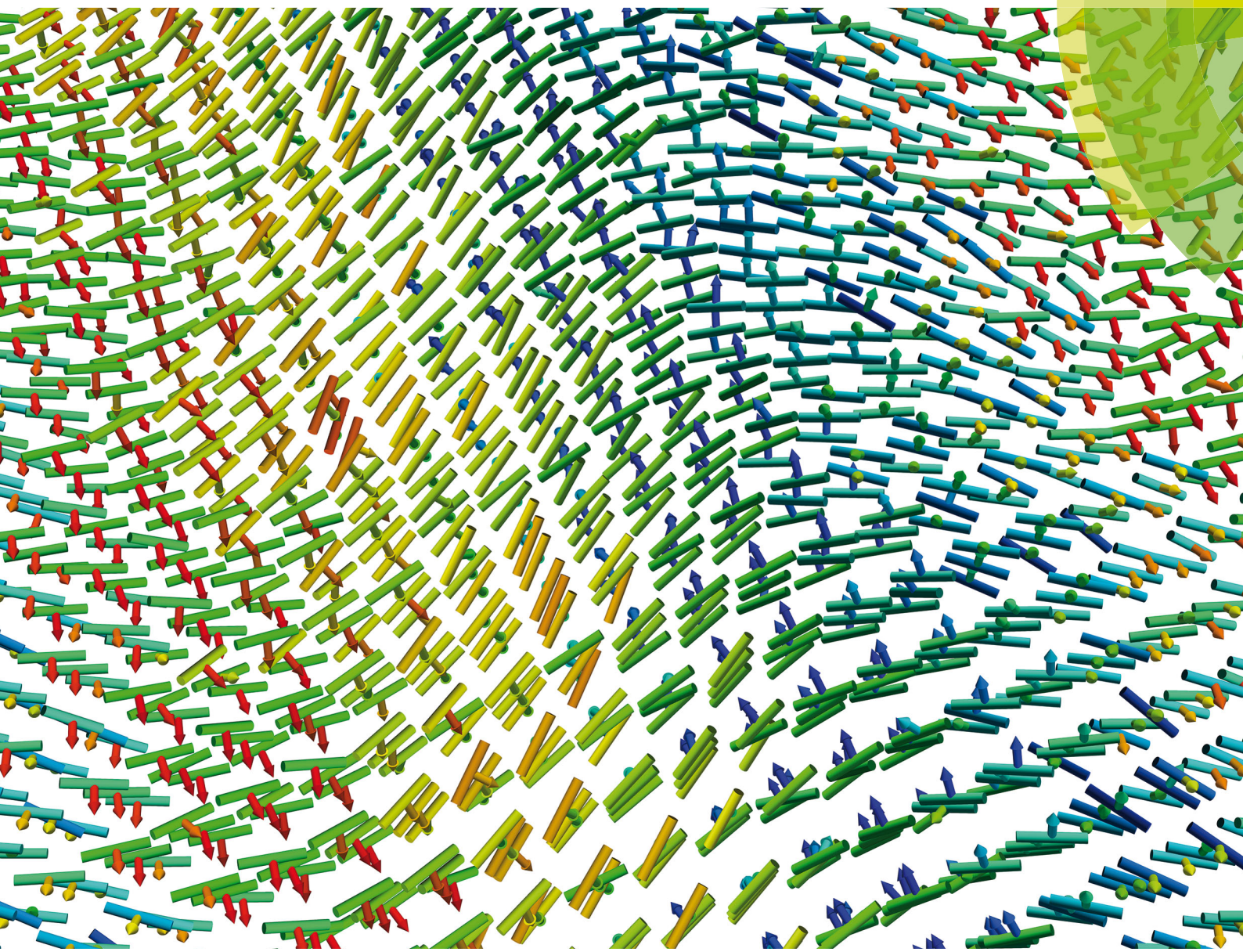

ISSN 1744-6848

ROYAL SOCIETY OF CHEMISTRY | Celebrating IYPT 2019

PAPER
Jonathan K. Whitmer *et al.*
Novel elastic response in twist-bend nematic models

Soft Matter

PAPER

View Article Online
View Journal | View Issue

Cite this: *Soft Matter*, 2019, **15**, 8219

Novel elastic response in twist-bend nematic models

Jiale Shi, Hythem Sidky and Jonathan K. Whitmer *

Received 10th July 2019,
Accepted 25th August 2019

DOI: 10.1039/c9sm01395d

rsc.li/soft-matter-journal

Bent-shaped liquid crystals have attracted significant attention recently due to their novel mesostructure and the intriguing behavior of their elastic constants, which are strongly anisotropic and have an unusual temperature dependence. Though theories explain the onset of the twist-bend nematic phase (N_{TB}) through spontaneous symmetry breaking concomitant with transition to a negative bend (K_3) elastic constant, this has not been observed as yet in experiments. There, the small bend elastic constant has a strongly non-monotonic temperature dependence, which first increases after crossing the isotropic (I)–nematic (N) transition, then dips near the nematic (N)-twist-bend (N_{TB}) transition before it increases again as the transition is crossed. The molecular mechanisms responsible for this exotic behavior are unclear. Here, we utilize density of states algorithms in Monte Carlo simulation applied to a variant of the Lebwohl–Lasher model which includes bent-shaped-like interactions to analyze the mechanism behind elastic response in this novel mesostructure and understand the temperature dependence of its Frank–Oseen elastic constants.

I. Introduction

Liquid crystals (LCs) are an intermediate phase between liquids and crystalline solids, having liquid-like positional order and solid-like orientational order. Since their discovery by Friedrich Reinitzer in 1888,[1] the innate responsiveness and anisotropic properties of LCs have found applications in many fields, including visual displays,[2,3] molecular machines,[4] nanoscale templating for self-assembly,[5] organic electronics,[6] chemical and biological sensing.[7–9] Perhaps the most well-known types of LCs are the nematic-phase (N) forming molecules that comprise the calamitic class. These are elongated, rod-like objects whose tendency to orientationally order has entropic origins,[10] though it is often reinforced by energetic concerns. However, these are not the only types of order.[11–14] As molecular species are nearly limitless, so too is the list of partially-ordered mesophases. Bent-shaped LCs,[11,14] sometimes descriptively called banana-shaped molecules,[15] can form one of these exotic phases, the twist-bend modulated nematic phase (N_{TB}),[16–20] and have demonstrated important responsive properties beyond the capabilities of simple nematics. A prototypical N_{TB}-former, CB7CB, is depicted in Fig. 1(a). The N_{TB} phase has microsecond linear optical response,[21,22] which has potential applications in fast optical response LCDs. N_{TB} phases have also been used as templates for photopolymerisation to form nano-heliconical structures with special electro-optical properties.[23]

Within N_{TB} phases, the elastic constants exhibit very intriguing behavior. First, they exhibit strongly anisotropic properties.[18,19,24] To be specific, the splay elastic constant K_1 is much larger than the bend elastic constant K_3. Second, the temperature dependence of K_3 is very unusual. With temperature decreasing, K_3 first increases after crossing the I–N transition, then dips near the N–N_{TB} transition, reversing and increasing again as the transition is crossed.[18,19,25–27] The origins of this peculiar effect have not yet been explained; indeed the behavior is at odds with the prevailing theoretical expectations.[28] Regarding origins of the

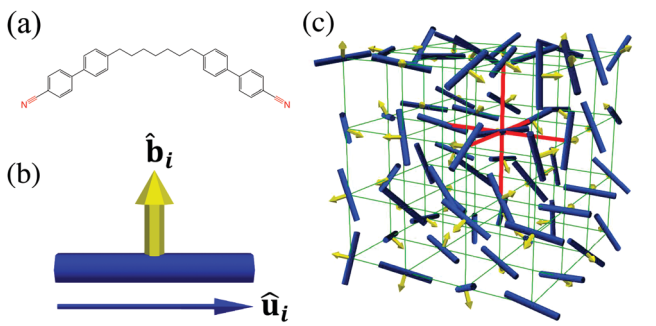

Fig. 1 (a) Structure of the CB7CB molecule, a prototypical bent-shaped mesogen. The two lobes of the molecule are similar to the commonly used cyanobiphenyl mesogen series *n*CB with each *n*CB attached at their terminal carbon. (b) An augmented Lebwohl–Lasher model[34] may be used to model bent-shaped models *via* the addition of a secondary orientation vector $\hat{\mathbf{b}}_i$ in addition to the standard orientation vector $\hat{\mathbf{u}}_i$ representing the long molecular axis of the molecules. This additional vector takes into account dipole-like signed interactions which arise from electronic structure or simply molecular shape. For simplicity, we work with a model where $\hat{\mathbf{b}}_i$ and $\hat{\mathbf{u}}_i$ are perpendicular. (c) Snapshot of part of typical Monte Carlo simulation of these bent-shaped liquid crystals. We utilize a cubic lattice with periodic boundary condition, where each site has six nearest neighbors with which to interact, denoted by the red lines.

Department of Chemical and Biomolecular Engineering, University of Notre Dame, Notre Dame, IN 46556, USA. E-mail: jwhitme1@nd.edu

N_{TB} phase, Meyer[29,30] was the first to suggest that spontaneous flexoelectric coupling between polarization and bend deformation would result in twist-bend heliconical structure. More recent theoretical work by Dozov[28] has posited that the twist-bend heliconical structure can originate from an elastic instability, where the effective bend elastic constant K_3 becomes negative. The mechanism for such a sign change is briefly discussed by Dozov, where it is mentioned that the effect need not rely on molecular polar ordering. While flexoelectric effects as considered by Meyer could be the origin of the N_{TB} phase, it could also be a more general ordering phenomenon, arising (*e.g.*) from packing concerns.[31] Though an unusual bend elastic response has been observed in systems of bent-shaped LCs, to date, no experiments have observed a negative value of K_3.[18,19,25,26] Sufficiently strong electrostatic or entropic polar interactions have been discussed as potential explanations for the reversal of the bend elastic constant near the onset of the N_{TB} phase.[28,32–34] It should be emphasized that though the mechanism is unknown, the prevailing theoretical attempts to explain this novel phase are strongly reliant on sign reversal of bend elasticity thus shifting the ground state of the LC from the nematic to a twist-bend phase within the Frank–Oseen (or, equivalently, the tensorial de Gennes) expression.

We seek to understand these unique elastic properties of bent-shaped molecules, and the role of polar forces in them, through molecular simulations. Lattice models,[34] coarse-grained models[31,35,36] and atomistic models[17,37] have been used to study the formation of heliconical twist-bend structures. While important aspects of the phase behavior and physical structure have been elucidated, these computational studies have not sought to connect molecular order to the exotic elasticity. Here, we perform a detailed study of the phase behavior and elastic response of bent-shaped LCs using an augmented Lebwohl–Lasher model[34] and free energy perturbation methods,[38] to connect the local orientational order underpinning the N_{TB} phase to its unusual elastic properties.

II. Model and simulation details

In the model, each bent-shaped molecule i is represented by two vectors[see Fig. 1(b)]. One defines the major axis of the molecule $\hat{\mathbf{u}}_i$, which aligns to form the nematic phase. The other is a polar vector $\hat{\mathbf{b}}_i$, aligned orthogonally to $\hat{\mathbf{u}}_i$, which is used to model local ordering interactions arising from electronic structure or geometrical shape. The volume is fixed and each pair of vectors is fixed in position and relative orientation, but allowed to rotate to seek favorable interactions with its six nearest neighbors [Fig. 1(c)] as determined by the Hamiltonian:[34]

$$\begin{aligned} H \;=\; & -\varepsilon \sum_{\langle i,j \rangle} \Big\{ A(\hat{\mathbf{u}}_i \cdot \hat{\mathbf{u}}_j)^2 + B_1(\hat{\mathbf{b}}_i \cdot \hat{\mathbf{b}}_j) + B_2(\hat{\mathbf{b}}_i \cdot \hat{\mathbf{b}}_j)^2 \\ & + \frac{C}{4}\Big\{(\hat{\mathbf{b}}_j \cdot \hat{\mathbf{u}}_i) \cdot \left[\hat{\mathbf{r}}_{ij} \cdot (\hat{\mathbf{u}}_i + \hat{\mathbf{u}}_j(\hat{\mathbf{u}}_i \cdot \hat{\mathbf{u}}_j))\right] \\ & - (\hat{\mathbf{b}}_i \cdot \hat{\mathbf{u}}_j) \cdot \left[\hat{\mathbf{r}}_{ij} \cdot (\hat{\mathbf{u}}_j + \hat{\mathbf{u}}_i(\hat{\mathbf{u}}_i \cdot \hat{\mathbf{u}}_j))\right]\Big\}\Big\}. \end{aligned} \tag{1}$$

The first term ($\propto A$) incorporates the standard Lebwohl–Lasher interaction, and promotes formation of a nematic phase. The second acts to align of dipoles in the same or opposing directions, depending on the sign of B_1. The third term ($\propto B_2$) allows for a secondary nematic order between the polar vectors. Finally, the fourth term couples the average polar environment with local bend-deformations.

In an extensive study,[34] the model was shown to permit nematic, polar nematic, biaxial nematic and twist-bend phases. Following ref. 34, we choose a set of parameters (A = 2.0, B_1 = 0.5, B_2 = 0.4, C = 2.0) which exhibits a N_{TB} phase at low temperatures. To balance accuracy with speed, we examined periodic bulk systems of various sizes, and settled on using $N = 16^3$ molecules, as the side length of the cube supports one complete helical turn of the twist-bend model that forms. In what follows, all quantities are presented in appropriate reduced units. Since timescales are not relevant, times and masses are not used. Energies E of the system, corresponding to evaluations of the Hamiltonian expression for a given microstate are defined relative to the constant energy scale ε *via* $E^* = E/\varepsilon$ and $T^* = k_B T/\varepsilon$, while lengths are defined relative to the lattice model's unit spacing a, so that $L^* = L/a$, $V^* = V/a^3$.

We implement the lattice Hamiltonian (eqn (1)) into the open-source Monte Carlo package SAPHRON,[39] and perform Monte Carlo simulations on fully periodic cubic systems with fixed side length $L^* = 16$ and thus fixed $N = V^* = 16^3$. The molecular vectors $\hat{\mathbf{u}}_i$ and $\hat{\mathbf{b}}_i$ attached to each lattice site are constrained to be orthogonal, and each molecule interacts only with its six nearest neighbors (see Fig. 1(c)). We utilize two different methods to obtain the phase behavior of this model. Initially, we perform canonical ensemble (*NVT*) to obtain equilibrated behavior starting from a random isotropic configuration at a temperature above the nematic–isotropic transition. In each Monte Carlo move, one lattice site i is chosen randomly, and a unit rotation matrix $\mathbf{R}$ is created by randomly choosing one among x, y, z axis to serve as the rotation axis and choosing a uniformly distributed random angle θ on the interval $[-\theta_{max}, \theta_{max}]$ which determines the extent of rotations. θ_{max} is optimized for each simulation between 1.0–3.0 radians to achieve $\approx$60% acceptance for rotations move at different temperatures, which promotes conformational exploration in both *NVT* and DOS sampling.[40] The matrix constructed from these variables is then applied to both unit vectors at each site.

$$\begin{aligned} \hat{\mathbf{u}}_i^{\text{new}} &= \mathbf{R} \cdot \hat{\mathbf{u}}_i^{\text{old}} \\ \hat{\mathbf{b}}_i^{\text{new}} &= \mathbf{R} \cdot \hat{\mathbf{b}}_i^{\text{old}} \end{aligned} \tag{2}$$

After rotating the molecule, the total energy difference of the system $\Delta E = E_2 - E_1$ is calculated, and moves are accepted according to the standard Metropolis criterion.[41] A set of sequential simulations is then carried out wherein the temperature is quenched from $T^* = 1.80$, and quenched to $T^* = 0.40$ in steps of $\Delta T^* = -0.01$, with each step performed using the protocol outlined above, with the final configuration of the simulation at each temperature serving as the initial configuration for the simulation at the next lower temperature.

Within these simulations, we monitor several thermodynamic and structural quantities, including the internal energy

per molecule $\langle U^* \rangle$, and constant volume heat capacity per molecule $\langle C_V^* \rangle$, defined by

$$\langle U^* \rangle = \left\langle \frac{E^*}{N} \right\rangle \tag{3}$$

$$\langle C_V^* \rangle = \frac{\left\langle \left(\frac{E^*}{N}\right)^2 \right\rangle - \left(\left\langle \frac{E^*}{N} \right\rangle\right)^2}{(T^*)^2}. \tag{4}$$

where N being the amount of molecules in the model. Additional quantities derived from the site orientation and Hamiltonian terms are also utilized to understand which types of global and local order are most prevalent at a given temperature. A polar order parameter,

$$\langle P \rangle = \left\langle \left| \frac{1}{N} \sum_{i=1}^{N} \hat{\mathbf{b}}_i \right| \right\rangle \tag{5}$$

records the magnitude of alignment of the polar vectors within the system. The nematic order S and director $\hat{\mathbf{n}}$ is captured through the largest eigenvalue and the corresponding eigenvector of the nematic ordering tensor $\mathbf{Q}$

$$\mathbf{Q} = \frac{1}{N} \sum_{i=1}^{N} \left(\frac{3}{2} \hat{\mathbf{u}}_i \hat{\mathbf{u}}_i - \frac{1}{2} \hat{\mathbf{I}} \right). \tag{6}$$

This tensor is used in two ways in the current study, to define global ordering, and to define regional ordering within the restriction and deformation regions used in elastic constant simulations.

We additionally compute a few specific terms within the Hamiltonian, which are defined by

$$\langle \beta_1 \rangle = \left\langle \frac{1}{3N} \sum_{\langle i,j \rangle} \left(\hat{\mathbf{b}}_i \cdot \hat{\mathbf{b}}_j \right) \right\rangle \tag{7}$$

$$\langle \beta_2 \rangle = \left\langle \frac{1}{3N} \sum_{\langle i,j \rangle} \left(\hat{\mathbf{b}}_i \cdot \hat{\mathbf{b}}_j \right)^2 \right\rangle \tag{8}$$

$$\begin{aligned} \langle \gamma \rangle \; = \Bigg\langle \frac{1}{3N} \sum_{\langle i,j \rangle} \Big\{ & (\hat{\mathbf{b}}_j \cdot \hat{\mathbf{u}}_i)[\hat{\mathbf{r}}_{ij} \cdot (\hat{\mathbf{u}}_i + \hat{\mathbf{u}}_j (\hat{\mathbf{u}}_i \cdot \hat{\mathbf{u}}_j))] \\ & - (\hat{\mathbf{b}}_i \cdot \hat{\mathbf{u}}_j)[\hat{\mathbf{r}}_{ij} \cdot (\hat{\mathbf{u}}_j + \hat{\mathbf{u}}_i (\hat{\mathbf{u}}_i \cdot \hat{\mathbf{u}}_j))] \Big\} \Bigg\rangle. \end{aligned} \tag{9}$$

These are useful for elucidating the origin of new ordered phases as we explore the N–N_{TB} transition region.

Following the initial simulations, we additionally apply Wang–Landau (WL) DOS sampling[42–44] to obtain the microcanonical partition function $\Omega(E,V,N)$ and use this as a way to validate and refine our temperature-sweep simulations; in particular, these can explore more sharply the behavior of $\langle U^* \rangle$ and $\langle C_V^* \rangle$. Each is accessible from standard statistical mechanical formulas once $\Omega(N,V,E)$ is known. Every canonical ensemble average $\langle X \rangle_{NVT}$ can be calculated by

$$\langle X \rangle_{NVT} = \frac{\sum_E X(E) \Omega(E) e^{-\beta E}}{\sum_E \Omega(E) e^{-\beta E}}, \tag{10}$$

which enables swift evaluation of $\langle U^* \rangle$ and $\langle C_V^* \rangle$ as quoted above.

Finally, as our ultimate interest is in the elastic free energy within the nematic phase of this model system, we perform expanded-ensemble simulations along deformation coordinates which isolate terms of the Frank–Oseen free energy,[45–47]

$$f_{FO} = \frac{1}{2} K_1 (\nabla \cdot \hat{\mathbf{n}})^2 + \frac{1}{2} K_2 (\hat{\mathbf{n}} \cdot \nabla \times \hat{\mathbf{n}})^2 + \frac{1}{2} K_3 (\hat{\mathbf{n}} \times \nabla \times \hat{\mathbf{n}})^2 \tag{11}$$

where K_1, K_2 and K_3 being the splay, twist, and bend elastic constants. The method has been utilized to explore the elasticity of lattice, coarse-grained, and atomistic models, and extensive descriptions are available elsewhere.[38,40,48–50] The order parameters for bend, twist, and splay are defined through tilting of the local nematic director as defined in ref. 38, 48 and 49 and expanded-ensemble density of states simulations[44,51] are subsequently applied to these variables. The resulting free energy landscape in the appropriate order parameter ξ may then be fit to a parabolic profile, allowing the elastic constant associated with that order parameter to be extracted from the relation $F/\varepsilon = \frac{1}{2} K^* \cdot V \cdot \xi^2$.

III. Results and discussion

To understand the elastic properties in this model, we must first map out its phase behavior and intrinsic order; these are plotted in the panels of Fig. 2. As previously noted, we can identify phase transitions through the dependence of reduced energy $\langle U^* \rangle$, and reduced heat capacity $\langle C_V^* \rangle$ [Fig. 2(a) and (b)]. Each calculation is performed in two ways: an initial temperature sweep beginning in the isotropic phase at $T^* = 1.80$ and quenching the system to $T^* = 0.40$ in steps of $\Delta T^* = -0.01$, followed by Wang–Landau sampling applied to the energy range observed in this sweep. The Wang–Landau portion is run until the convergence factor reaches $\mathcal{O}(10^{-8})$, and serves to confirm and refine our understanding of the model's thermodynamics. Three phase transitions are identified this way, with the isotropic–nematic (IN) transition at $T_{IN}^* = 1.56$ the most prominent. Cooling to $T^* = 1.33$, a second peak is present, defining a transition from the nematic state N to an as-yet unknown nematic state N_X. Finally, at $T^* = 1.20$, a final transition is seen to the twist-bend nematic phase N_{TB} which was observed for these parameters in ref. 34.

To elucidate the microstructural changes, we plot in Fig. 2(c)–(f) the set of structural order parameters outlined in the previous section. Data for these simulations is gathered from the constant-temperature simulations performed at each stage of the temperature sweep. Examining first the polarization $\langle P \rangle$ in Fig. 2(c), we note that the value is relatively small

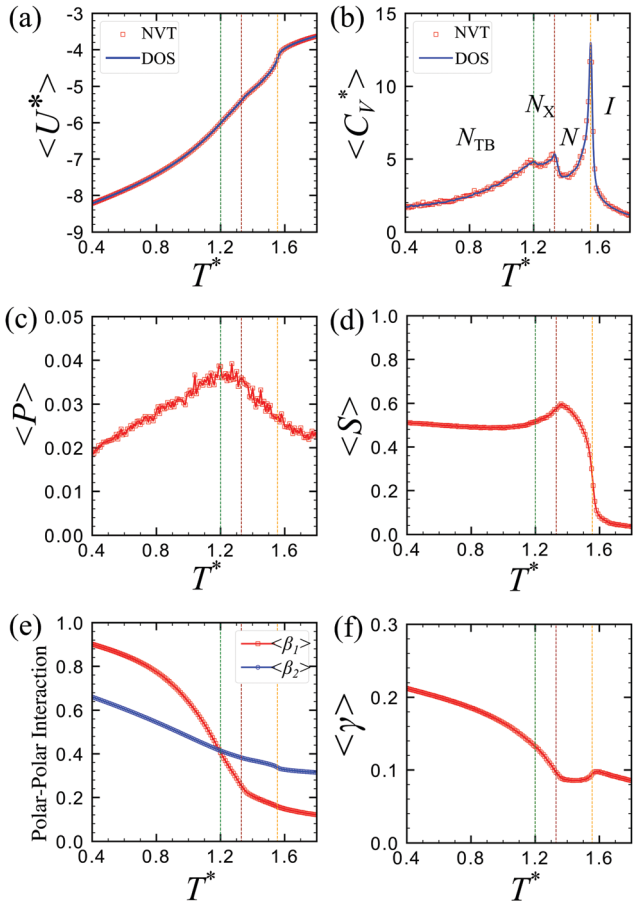

Fig. 2 Phase behavior of the augmented LL model system, examined using Wang–Landau density of states (DOS) and canonical ensemble simulations (*NVT*). The thermodynamics and order within the system are plotted as a function of reduced temperature T^* for (a) internal energy $\langle U^* \rangle$, (b) heat capacity $\langle C_V^* \rangle$, (c) global polar order parameter $\langle P \rangle$, (d) global nematic order parameter $\langle S \rangle$, and energetic contributions from polar (e) and twist-bend (f) interactions in the Hamiltonian, which serve as additional order parameters $\langle \beta_1 \rangle, \langle \beta_2 \rangle, \langle \gamma \rangle$. The model exhibits three phase transitions, which are indicated by vertical dashed lines on each panel; the isotropic–nematic transition occurs at $T_{IN}^* = 1.56$ (orange), while a nematic-modulated nematic transition occurs $T_{NN_X}^* = 1.33$ (brown) and finally a transition to a twist-bend phase occurs at $T_{N_XN_{TB}}^* = 1.20$ (green). The heat capacity plotted in (b) most dramatically demonstrates three peaks corresponding to orientational ordering transitions.

throughout the full range of temperatures, indicating none of the observed phases are globally polar. However, polar order increases steadily until the third phase transition, after which it decreases. This indicates polar order is likely locally present in clusters which eventually become suppressed by the global twist-bend phase. The nematic order parameter $\langle S \rangle$ in Fig. 2(d) likewise shows an interesting dependence on temperature, where it increases sharply at the I–N transition until reaching the N_X phase, then decreases steadily until the material is well below the transition to the N_{TB} phase.

To further understand the impact of specific interactions and orderings on low-temperature phase transitions, we analyze the average contributions of individual terms in the Hamiltonian (1) in Fig. 2(e) and (f). Importantly, we see an increase in *local* polar interaction $\langle \beta_1 \rangle$ at the second phase transition, to the point where its contributions outweigh those of the biaxial–nematic term $\langle \beta_2 \rangle$ at the third phase transition. This hints that local polar ordering is important in these transitions, with local clustering eventually dominated by the fully modulated phase upon cooling.[28,32–34] Due to its sharp increase after transition from N to N_X, $\langle \beta_1 \rangle$ appears to act as a stabilising factor to N_{TB}, where polar interactions have been hypothesized to be important in the onset of the phase.[28,32,33] The biaxial nematic-like term, $\langle \beta_2 \rangle$ (Fig. 2(e)), increases linearly in N, N_X and N_{TB} while T^* decreases. Importantly, when proper scaling is taken into account, it is seen that the value increases from a disordered-like state, to one where there is a measure of local nematic order for the polar vectors, though it never becomes perfectly aligned. This is expected, since the chiral pitch engendered by the N_{TB} phase will prevent global biaxial ordering. Finally, we also plot $\langle \gamma \rangle$ which enforces parallel alignment of polar order and local bend (Fig. 2(f)), and find that it displays an exotic temperature dependence. To be specific, it decreases slightly after crossing the I–N transition then starts to increase again before the N–N_X transition, where it once again begins to increase dramatically at temperatures below the N–N_X transition. Intriguingly, we find no sharp changes of order parameters at $T_{N_XN_{TB}}^*$, leading us to hypothesize that the N_X phase is a twist-bend phase where the nematic axis tilt angle is growing[52] and is frustrated by the rigid boundaries of our finite sized system, with the angle ultimately stabilizing at the low-temperature transition point $T_{N_XN_{TB}}^* = 1.20$.

Data supporting this perspective is presented in Fig. 3–5. We plot the local order of both $\hat{\mathbf{n}}$ [panels (a, c, e and g)] and $\hat{\mathbf{b}}$ [panels (b, d, f, h)] of each layer for specific temperatures within each phase. Directors are assumed to be oriented in the upper half-plane to remove head–tail effects; no restrictions are placed on $\hat{\mathbf{b}}$ vectors. This confirms that at the onset of the N_X phase, modulated order is present in both $\hat{\mathbf{n}}$ and $\hat{\mathbf{b}}$, as is expected for the twist-bend phase.[28,30] The pitch in both cases matches the box size, though the amplitude of modulations is much larger at low temperatures when fluctuations are damped. Indeed, in both low-temperature phases heliconical structure[18,19,28] is observed. From the images in Fig. 4 and 5 it is clear that the modulation in the N_X phase is not as strong, with the average local director deviating only slightly from the presumed heliconical axis z. This is commensurate with an increased tilt angle, which permits formation of a periodic heliconical phase. Experimental results[52] have shown existence of a continuously increasing tilt angle after crossing $T_{NN_{TB}}$ which eventually saturates. Because of this, we anticipate that the transition taking place at $T^* = 1.33$ is representative of the N–N_{TB} transition.

Though the effects are small, one can observe a slight difference in the modulation of the z-component of $\hat{\mathbf{n}}$ in the higher temperature phase, indicating potential frustration of otherwise twist-bend-like order with the finite box size in Fig. 6. Experiments have observed in twist-bend forming LCs that the periodicity of the system can also change as temperature decreases.[17,53] Though this is not possible in our system due to the fixed lattice size, we hypothesize that the system can

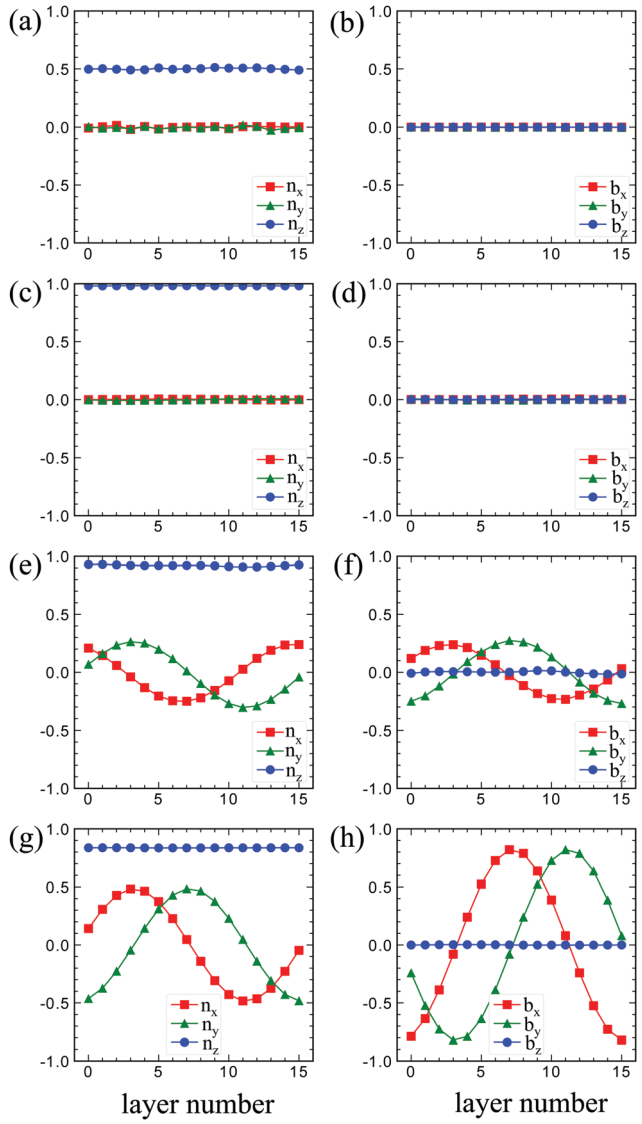

Fig. 3 Average Cartesian projections of the nematic ($\hat{\mathbf{n}}$) and polar ($\hat{\mathbf{b}}$) ordering vectors within slices of constant z at different state points: (a and b) T^* = 1.70, isotropic phase (I); (c and d) T^* = 1.45, nematic phase (N); (e and f) T^* = 1.27, N_X phase; (g and h) T^* = 0.50, twist-bend phase (N_{TB}).

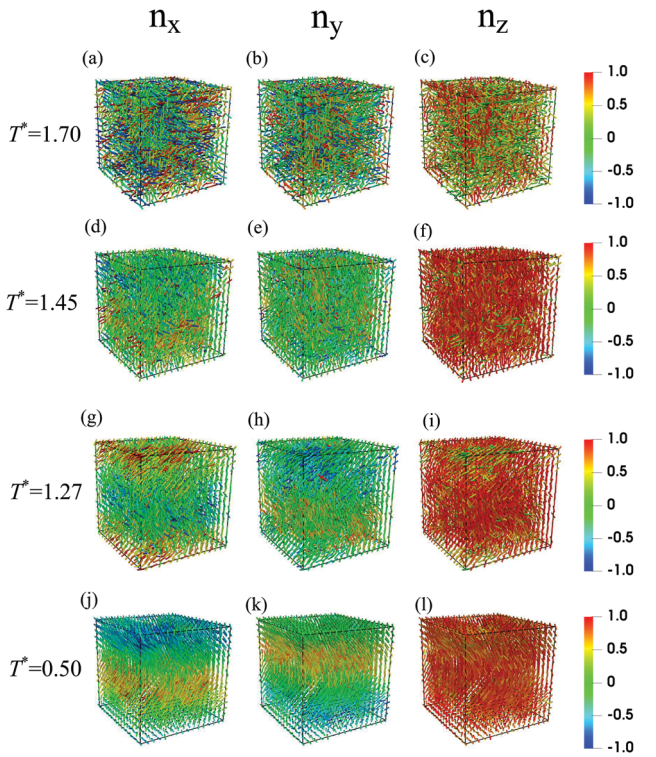

Fig. 4 Snapsots from simulation corresponding to the temperatures and conditions in Fig. 3, display the projection of the local nematic axis $\hat{\mathbf{n}}$ on x, y, and z from left to right. (a–c) T^* = 1.70, isotropic phase (I); (d–f) T^* = 1.45, nematic phase (N); (g–i) T^* = 1.27, N_X phase; (j–l) T^* = 0.50, twist-bend phase (N_{TB}).

partially relieve frustrations induced by the fixed lattice size by tilting the heliconical axis away from the z direction, which would induce a modulation of n_z as well. As we observe in Fig. 6, the N_X phase shows significant deviation from a uniform director component along z, which is present in both the general nematic phase N and the twist-bend phase N_{TB}. Importantly, while the projected director $\hat{\mathbf{n}}\cdot\hat{\mathbf{z}}$ is very uniform among layers in the N and N_{TB} phases, maintaining a stable heliconical tilt in the latter, this is not uniform within the N_X phase, indicating a tilt structure is formed in N_X which is intermediate between the two, and slightly misaligned with the z axis. Therefore, we conclude the N_X phase is effectively a twist bend phase that is frustrated by the limited size of our simulation box. This supports our hypothesis of a varying heliconical pitch, as the nematic director exhibits modulation within the N_X region of the phase diagram. The onset of tilting is also indirectly evident in the trend of nematic order S from Fig. 2(d), as the N_X phase coincides with a drop in overall nematic ordering which is partially recovered in the N_{TB} phase when axis and tilt angle stabilize. We hypothesize the N to N_X to N_{TB} sequence of phase transitions observed here will be replaced by a single N to N_{TB} in sufficiently large or off-lattice systems.

Having established the phase behavior, we proceed to explore the temperature dependence of elastic constants K_i, The resulting temperature dependence of the reduced elastic constants K_1^*, K_2^*, K_3^* is shown in Fig. 7. It is apparent that the reduced elastic constants in this model are strongly anisotropic, demonstrating bend K_3^* to be much weaker than splay K_1^* and twist K_2^*, which are approximately the same. The relative similarity of K_2^* and K_1^* may be rationalized from the lack of terms coupling the polar vector $\hat{\mathbf{b}}$ to splay and twist, and the fact that the standard Lebwohl–Lasher model exhibits only a single elastic constant. This similarity to the standard Lebwohl–Lasher model also extends to the temperature dependence of K_1^* and K_2^*.

Such similarity does not extend to K_3^*, which in addition to its reduced value, shows unusual nonmonotonic behavior. Upon crossing T_{IN}, K_3^* first rises, then falls off near zero, only to rise again approaching the transition to the N_X phase. This is reminiscent of experimental measurements of twist-bend elasticity which measured nonmonotonic behavior approaching

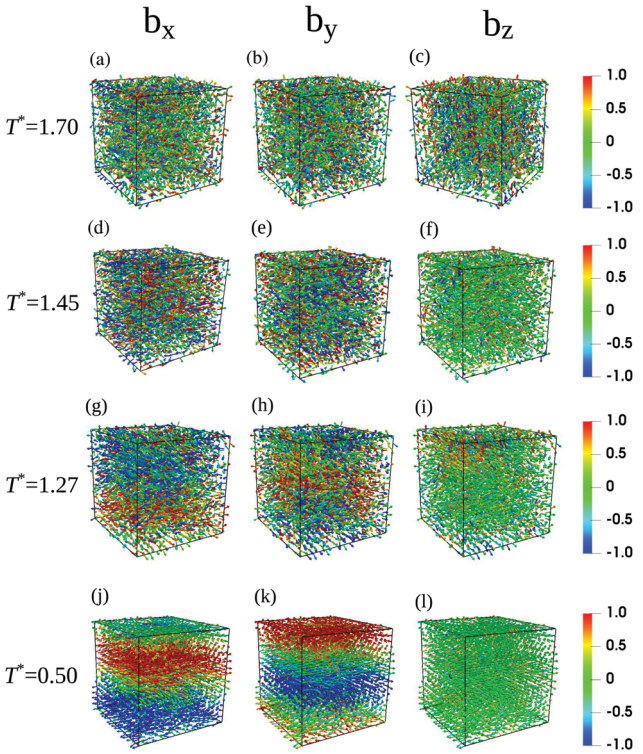

Fig. 5 Snapshots from simulation corresponding to the temperatures and conditions in Fig. 3, display the projection of the local polar axis $\hat{\mathbf{b}}$ on *x*, *y*, and *z* from left to right. (a–c) I phase, T^* = 1.70, (d–f) is N phase, T^* = 1.45, (g–i) N_X phase, T^* = 1.27, (j–l) N_{TB} phase, T^* = 0.50.

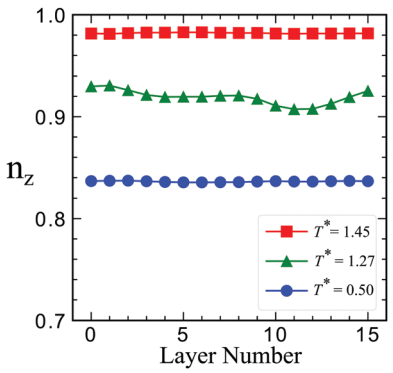

Fig. 6 Projected nematic director n_z within slices of constant *z* at different state points for three temperatures analysed in Fig. 3. T^* = 1.45 (red, N phase); T^* = 1.27 (green, N_X phase) and T^* = 0.50 (blue, N_{TB} phase).

the twist bend phase from the nematic, with a prominent uptick in elastic constant immediately preceding the transition.[18,19,26,54] Importantly, both our results and prior experiments are at odds with the prevailing theoretical picture[28,55] where K_3* must become negative approaching the twist-bend phase.

Note that the polar interactions and bend coupling term imposed here likely play a prominent role in the interesting behavior of the K_3* elastic constant. These augmented interactions allow a system to rearrange their polar vectors in order to absorb some of the strain from the bend deformation.

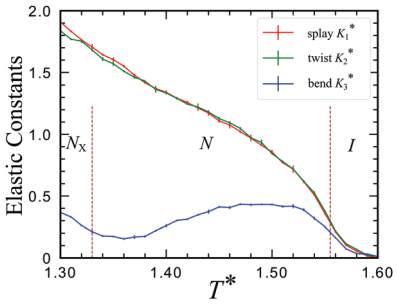

Fig. 7 The bulk elastic constants, splay K_1* (red), twist K_2* (green), and bend K_3* (blue), for the bent-shaped Lebwohl–Lasher model in the nematic phase. The elastic constants are strongly anisotropic, with K_1* and K_2* much larger than K_3*, as seen in experiments examining the nematic elastic behavior of twist-bend-forming mesogens. While twist and splay exhibit similar behavior to the standard Lebwohl–Lasher model, bend K_3* has an unusual temperature dependence. When T^* decreases, K_3* first increases up to a point, and then decreases as T_{NN_X} is approached. Near this transition, it begins to increase again. Both the strongly anisotropic elasticity and unusual temperature dependence of K_3*, when taken together are suggestive that the phase behavior has a strong influence on the apparent elastic constants measured, dependencies in experimental systems.[18,19,26]

Such a perspective is supported by experimental results. Cukrov and co-workers[26] noted that the unusual behaviors of the elastic constants show a strong temperature dependence that can be associated with bend-induced changes in the orientational distribution function. Importantly, these interactions are not strong enough to shift the ground state of the LC to an equilibrium deformed state until the system crosses through $T_{NN_{TB}}$. We thus hypothesize that local order can be influenced significantly by these polar interactions as the transition is approached, leading to the creation of clusters that stiffen the bend response.

Having demonstrated this behavior, it is beneficial to place it in the context of prior theoretical results. Prior results examining the role of flexoelectricity, including ref. 32 and 33, showed that this effect could contribute to the formation of a twist-bend phase, and that concomitantly this results in an effective K_3 which changed sign. This conflicts with the experimental results of ref. 18, 19 and 26, and with our observations in this model, where the effective elastic constant remains positive, and actually begins to increase near the N–N_{TB} transition, even though this model explicitly includes polar interactions and coupling terms between the polar vectors and primary mesogen axis, which defines the nematic ordering. However, it is not clear that it necessarily supports competing theoretical models expanding the Frank free energy[56] which do not require the value of K_3 to change sign, provided other elastic terms have values which appropriately compensate for the cost of intrinsic elastic deformations. The key difference is that those methods regard K_3 as an intrinsic property and do not consider the effective K_3 which is measured in experiments, and in our simulations. What our results point to is an incomplete theoretical picture that needs to be further elucidated by directed experiments and simulations.

IV. Conclusion

We have studied the dependence of nematic elastic constants on the phase behavior for an augmented Lebwohl–Lasher model modified to incorporate twist-bend ordering. While the model is simple, the obtained elastic constants nevertheless have qualitative properties and nontrivial temperature dependences in accord with experimental results reported in bent-shaped LCs,[18,19,26,57] which have obvious anisotropic properties. More importantly, the initially cheap bend elastic constant decreases to a very small value close to the N–N_{TB} phase transition. We observe that the polar and twist-bend coupling terms are the dominant effects in novel elastic behavior near this transition. Our results unequivocally demonstrate the role of polar ordering in decreasing the bend elastic constant, and the role of polar ordering and polar–nematic coupling associated with shape-dipole-like terms in the onset of the eventual twist-bend phase. This work will enable the design of bespoke materials with sensitive, large-bend anisotropy and strong optical responses near the N_{TB} phase transition.[21,22]

Conflicts of interest

There are no conflicts to declare.

Acknowledgements

J. S. and J. K. W. acknowledge support from the Midwest Integrated Center for Computation of Materials (MICCoM), as part of the Computational Materials Sciences Program funded by the U.S. Department of Energy, Office of Science, Basic Energy Sciences, Materials Sciences and Engineering Division. J. S. and J. K. W. acknowledge computational resources at the Notre Dame Center for Research Computating (CRC). H. S. acknowledges support from the National Science Foundation Graduate Research Fellowship Program (NSF-GRFP). J. S. thanks Dr Vikramjit Rathee and Michael Quevillon for help with visualization.

References

1 F. Reinitzer, *Monatsh. Chem. Verw. Teile Anderer Wiss.*, 1888, **9**, 421–441.
2 B. Bahadur, *Mol. Cryst. Liq. Cryst.*, 1984, **109**, 3–93.
3 G. W. Gray and S. M. Kelly, *J. Mater. Chem.*, 1999, **9**, 2037–2050.
4 T. Orlova, F. Lancia, C. Loussert, S. Iamsaard, N. Katsonis and E. Brasselet, *Nat. Nanotechnol.*, 2018, **13**, 304.
5 X. Li, J. C. Armas-Pérez, J. P. Hernández-Ortiz, C. G. Arges, X. Liu, J. A. Martinez-Gonzalez, L. E. Ocola, C. Bishop, H. Xie, J. J. de Pablo and P. F. Nealey, *ACS Nano*, 2017, **11**, 6492–6501.
6 V. G. Nazarenko, O. P. Boiko, M. I. Anisimov, A. K. Kadashchuk, Y. A. Nastishin, A. B. Golovin and O. D. Lavrentovich, *Appl. Phys. Lett.*, 2010, **97**, 263305.
7 R. J. Carlton, J. T. Hunter, D. S. Miller, R. Abbasi, P. C. Mushenheim, L. N. Tan and N. L. Abbott, *Liq. Cryst. Rev.*, 2013, **1**, 29–51.
8 Q. Li, *Liquid Crystals Beyond Displays: Chemistry, Physics, and Applications*, John Wiley & Sons, 2012.
9 S. Yang, C. Wu, H. Tan, Y. Wu, S. Liao, Z. Wu, G. Shen and R. Yu, *Anal. Chem.*, 2012, **85**, 14–18.
10 L. Onsager, *Ann. N. Y. Acad. Sci.*, 1949, **51**, 627–659.
11 H. Takezoe and A. Eremin, *Bent-Shaped Liquid Crystals: Structures and Physical Properties*, CRC Press, 2017.
12 D. Andrienko, *J. Mol. Liq.*, 2018, **267**, 520–541.
13 R. J. Mandle, *Chem. Rec.*, 2018, **18**, 1341–1349.
14 A. Jákli, O. D. Lavrentovich and J. V. Selinger, *Rev. Mod. Phys.*, 2018, **90**, 045004.
15 T. Niori, T. Sekine, J. Watanabe, T. Furukawa and H. Takezoe, *J. Mater. Chem.*, 1996, **6**, 1231–1233.
16 M. Cestari, S. Diez-Berart, D. A. Dunmur, A. Ferrarini, M. R. de la Fuente, D. J. B. Jackson, D. O. Lopez, G. R. Luckhurst, M. A. Perez-Jubindo, R. M. Richardson, J. Salud, B. A. Timimi and H. Zimmermann, *Phys. Rev. E: Stat., Nonlinear, Soft Matter Phys.*, 2011, **84**, 031704.
17 D. Chen, J. H. Porada, J. B. Hooper, A. Klittnick, Y. Shen, M. R. Tuchband, E. Korblova, D. Bedrov, D. M. Walba, M. A. Glaser, J. E. Maclennan and N. A. Clark, *Proc. Natl. Acad. Sci. U. S. A.*, 2013, **110**, 15931–15936.
18 V. Borshch, Y.-K. Kim, J. Xiang, M. Gao, A. Jákli, V. P. Panov, J. K. Vij, C. T. Imrie, M.-G. Tamba, G. H. Mehl and O. D. Lavrentovich, *Nat. Commun.*, 2013, **4**, 3635.
19 G. Babakhanova, Z. Parsouzi, S. Paladugu, H. Wang, Y. A. Nastishin, S. V. Shiyanovskii, S. Sprunt and O. D. Lavrentovich, *Phys. Rev. E*, 2017, **96**, 062704.
20 C. Greco, A. Ferrarini, G. R. Luckhurst, B. A. Timimi and H. Zimmermann, *Liq. Cryst.*, 2018, **45**, 2361–2375.
21 V. P. Panov, R. Balachandran, M. Nagaraj, J. K. Vij, M. G. Tamba, A. Kohlmeier and G. H. Mehl, *Appl. Phys. Lett.*, 2011, **99**, 261903.
22 S. P. Sreenilayam, Y. P. Panarin, J. K. Vij, V. P. Panov, A. Lehmann, M. Poppe, M. Prehm and C. Tschierske, *Nat. Commun.*, 2016, **7**, 11369.
23 V. P. Panov, S. P. Sreenilayam, Y. P. Panarin, J. K. Vij, C. J. Welch and G. H. Mehl, *Nano Lett.*, 2017, **17**, 7515–7519.
24 K. L. Atkinson, S. M. Morris, F. Castles, M. M. Qasim, D. J. Gardiner and H. J. Coles, *Phys. Rev. E: Stat., Nonlinear, Soft Matter Phys.*, 2012, **85**, 012701.
25 K. Adlem, M. Čopičc, G. R. Luckhurst, A. Mertelj, O. Parri, R. M. Richardson, B. D. Snow, B. A. Timimi, R. P. Tuffin and D. Wilkes, *Phys. Rev. E: Stat., Nonlinear, Soft Matter Phys.*, 2013, **88**, 022503.
26 G. Cukrov, Y. Mosaddeghian Golestani, J. Xiang, Y. A. Nastishin, Z. Ahmed, C. Welch, G. H. Mehl and O. D. Lavrentovich, *Liq. Cryst.*, 2017, **44**, 219–231.
27 Z. Parsouzi, G. Babakhanova, M. Rajabi, R. Saha, P. Gyawali, T. Turiv, H. Wang, A. R. Baldwin, C. Welch, G. H. Mehl, J. T. Gleeson, A. Jakli, O. D. Lavrentovich and S. Sprunt, *Phys. Chem. Chem. Phys.*, 2019, **21**, 13078–13089.
28 I. Dozov, *Europhys. Lett.*, 2001, **56**, 247.

29 R. B. Meyer, in *Les Houches Summer School in Theoretical Physics*, 1973, ed. R. Balian and G. Weil, Molecular Fluids, Gordon and Breach, New York, 1976, pp. 273–373.
30 R. B. Meyer, *Mol. Cryst. Liq. Cryst.*, 1977, **40**, 33–48.
31 C. Greco and A. Ferrarini, *Phys. Rev. Lett.*, 2015, **115**, 147801.
32 M. A. Osipov and G. Pajak, *Eur. Phys. J. E: Soft Matter Biol. Phys.*, 2016, **39**, 45.
33 M. A. Osipov and G. Pajak, *Liq. Cryst.*, 2017, **44**, 58–67.
34 S. M. Shamid, S. Dhakal and J. V. Selinger, *Phys. Rev. E: Stat., Nonlinear, Soft Matter Phys.*, 2013, **87**, 052503.
35 R. Memmer, *Liq. Cryst.*, 2002, **29**, 483–496.
36 A. G. Vanakaras and D. J. Photinos, *Liq. Cryst.*, 2018, **45**, 2184–2196.
37 X. Wei, PhD thesis, The University of Utah, 2016.
38 A. A. Joshi, J. K. Whitmer, O. Guzmán, N. L. Abbott and J. J. de Pablo, *Soft Matter*, 2014, **10**, 882–893.
39 H. Sidky and J. S. Benjamin, *SAPHRON - A Lightweight C + +11 Monte Carlo Molecular Simulation Engine*, 2016, https://github.com/hsidky/SAPHRON.
40 H. Sidky and J. K. Whitmer, *Liq. Cryst.*, 2016, **43**, 2285–2299.
41 D. Frenkel and B. Smit, *Understanding Molecular Simulation: From Algorithms to Applications*, Elsevier, 2002, vol. 1.
42 F. Wang and D. P. Landau, *Phys. Rev. Lett.*, 2001, **86**, 2050–2053.
43 D. P. Landau, S.-H. Tsai and M. Exler, *Am. J. Phys.*, 2004, **72**, 1294–1302.
44 S. Singh, M. Chopra and J. J. de Pablo, *Annu. Rev. Chem. Biomol. Eng.*, 2012, **3**, 369–394.
45 M. Kleman and O. D. Laverntovich, *Soft Matter Physics: An Introduction*, Springer Science & Business Media, 2001.
46 P. G. de Gennes and J. Prost, *The Physics of Liquid Crystals*, Oxford University Press, 1995, vol. 83.
47 I. W. Stewart, *The Static and Dynamic Continuum Theory of Liquid Crystals*, Taylor and Francis, London, 2004, vol. 17.
48 J. K. Whitmer, C.-c. Chiu, A. A. Joshi and J. J. de Pablo, *Phys. Rev. Lett.*, 2014, **113**, 190602.
49 H. Sidky and J. K. Whitmer, *Soft Matter*, 2016, **12**, 4489–4498.
50 H. Sidky, J. J. de Pablo and J. K. Whitmer, *Phys. Rev. Lett.*, 2018, **120**, 107801.
51 E. B. Kim, R. Faller, Q. Yan, N. L. Abbott and J. J. de Pablo, *J. Chem. Phys.*, 2002, **117**, 7781–7787.
52 C. Meyer, G. R. Luckhurst and I. Dozov, *J. Mater. Chem. C*, 2015, **3**, 318–328.
53 M. R. Tuchband, M. Shuai, K. A. Graber, D. Chen, C. Zhu, L. Radzihovsky, A. Klittnick, L. M. Foley, A. Scarbrough, J. H. Porada, M. Moran, J. Yelk, D. Bedrov, E. Korblova, D. M. Walba, A. Hexemer, J. E. Maclennan, M. A. Glaser and N. A. Clark, 2017, arXiv preprint arXiv:1703.10787.
54 D. O. López, B. Robles-Hernández, J. Salud, M. R. De la Fuente, N. Sebastian, S. Diez-Berart, X. Jaen, D. A. Dunmur and G. R. Luckhurst, *Phys. Chem. Chem. Phys.*, 2016, **18**, 4394–4404.
55 I. Lelidis and G. Barbero, *J. Mol. Liq.*, 2019, **275**, 116–121.
56 G. Barbero, L. R. Evangelista, M. P. Rosseto, R. S. Zola and I. Lelidis, *Phys. Rev. E: Stat., Nonlinear, Soft Matter Phys.*, 2015, **92**, 030501.
57 A. Aluculesei, H. Cachitas, J. Carvalho, F. V. Chavez, J. L. Figueirinhas, P. J. Sebastião, C. Cruz, M. G. Tamba, A. Kohlemeir and G. H. Mehl, *Phys. Chem. Chem. Phys.*, 2019, **21**, 4523–4537.